Nano Research

ISSN 1998-0124 CN 11-5974/O4
https://doi.org/10.1007/s12274-019-2579-1

Research Article

Solid-solution alloy nanoclusters of the immiscible gold-rhodium system achieved by a solid ligand-assisted approach for highly efficient catalysis

Xinchun Yang[1,2], Zhangpeng Li[1], Mitsunori Kitta[1], Nobuko Tsumori[3], Wenhan Guo[4], Zitao Zhang[4], Jianbo Zhang[5], Ruqiang Zou[4] (✉), and Qiang Xu[1,2,6] (✉)

[1] *Institute of Electrochemical Energy, National Institute of Advanced Industrial Science and Technology (AIST), Ikeda, Osaka 563-8577, Japan*
[2] *Graduate School of Engineering, Kobe University, Nada Ku, Kobe, Hyogo 657-8501, Japan*
[3] *Department of Applied Chemistry and Chemical Engineering, Toyama National College of Technology, Toyama 939-8630, Japan*
[4] *Department of Materials Science and Engineering, Peking University, Beijing 100871, China*
[5] *Centre for High-Pressure Science and Technology Advanced Research, Beijing 100094, China*
[6] *AIST-Kyoto University Chemical Energy Materials Open Innovation Laboratory, Yoshida, Sakyo-ku, Kyoto 606-8501, Japan*

Received: 30 October 2019 / **Revised:** 21 November 2019 / **Accepted:** 22 November 2019

ABSTRACT

Striking effects are expected in solid-solution alloying, which offers enormous possibilities for various applications, especially in industrial catalysis. However, phase diagrams have revealed that a wide range of metallic elements are immiscible with each other even above their melting points. Achieving such unknown alloying between different immiscible metallic elements is highly desirable but challenging. Here, for the first time, by using an innovative solid ligand-assisted approach, we achieve the solid-solution alloying between the bulk-immiscible Au and Rh in plenty of clean, ultrafine (~ 1.6 nm) and highly dispersed nanoclusters. The solid-solution alloying of immiscible Au and Rh significantly enhances their catalytic performance toward the hydrogen evolution from formic acid in contrast to the monometallic Au and Rh nanoclusters. Moreover, the resultant binary solid-solution nanoclusters are stable without any segregation during catalytic reactions. The approach demonstrated here for homogeneously mixing the immiscible metals at the atomic scale will benefit the creation of advanced alloys and their catalytic applications in future.

KEYWORDS

solid-solution alloys, metal nanoclusters, formic acid dehydrogenation, heterogeneous catalysis

1 Introduction

The chemistry of solid-solution alloying, as modern-day alchemy, opens enormous possibilities for many applications including optics, electronics, mechanics, biomedicine, and especially industrial catalysis, owing to the widely tunable structures and compositions, and the strong intermetallic synergistic interactions, which occur from the atomic interaction of different metals and usually lead to an enhanced intrinsic performance because of both geometric and electronic effects [1–6]. High-performance solid-solution alloys are heavily reliant on the well-defined miscible metallic elements up to now, whereas phase diagrams have revealed that many metallic elements are immiscible with each other even above their melting points [7–9]. Recently, significant progresses in both theoretical and experimental studies have demonstrated that phase segregation in bulk alloys could be restricted in nanostructured metals, often achieved by organic stabilizers, on account of the size-dependence effect [10–13]. However, issues have been encountered in this process that the use of organic capping agents at high temperature and pressure may produce large, segregated and unstable particles with limited synergistic interactions and blocked surfaces lacking accessible active sites to reactants, resulting in the loss of catalytic activities.

An ideal way to boost metals' catalytic activity is via anchoring metal clusters (MCs) with sizes less than 2 nm on solid supports, such as porous carbons, metal oxides, metal–organic frameworks (MOFs), covalent organic frameworks (COFs) and organic cages, on the basis of their distinct advantages: The clean surface and ultrafine size of supported MCs allow most of their constituent atoms to be exposed as accessible active sites [14–19]. Although supported MCs consisting of one element or two miscible elements have been well-demonstrated as excellent heterogeneous catalysts, to the best of our knowledge, there are few reports on the supported solid-solution alloy clusters consisting of bulk-immiscible metals, due to their great synthetic difficulties.

Emerging as a new class of functional materials, functionalized carbons synthesized by post-synthetic modification of carbons with functional groups have shown a broad scope of applications due to their high surface area, conductivity and thermal stability [20–25]. One particular use of functionalized carbons is to stabilize metal nanoparticles (MNPs), where C=O or C–N sites act as the MNP nucleation and growth sites. Intriguingly, some functionalized carbons can immobilize MCs and even single metal atoms. As Beller and co-workers have proposed, functionalized carbons in this case serve as solid ligands because

Address correspondence to Ruqiang Zou, rzou@pku.edu.cn; Qiang Xu, q.xu@aist.go.jp

the acquisition of isolated metal species involves the formation of complexes between metal precursors and N sites [23]. Monometallic Au and Rh have been used as efficient catalysts in various chemical reactions [26–28]. However, there are few systematic investigations for Au-Rh alloys owing to the large immiscibility gap between Au and Rh as predicted by the phase diagram, even in the liquid phase above 2,139 K [29]. Herein, we demonstrate a solid ligand-assisted methodology for the first time that, through significantly enhancing the chemical binding ability and electrostatic adsorption of the two metal precursors to an innovative solid ligand, can achieve the solid-solution alloying of the bulk-immiscible Au and Rh in plenty of clean, ultrafine (~ 1.6 nm) and highly dispersed nanoclusters at room temperature (Fig. 1). The pyridinic N/N–H sites act as N ligands for chemical binding while the C=O and OH groups provide surface charges for electrostatic adsorption; no additional capping agents are needed. Surprisingly, the obtained Au-Rh solid-solution alloy nanoclusters possess an extremely enhanced catalytic activity toward the hydrogen evolution from formic acid (HCOOH, FA) compared to their monometallic parents, i.e., Au becomes more active when contacted with Rh, even though the latter is catalytically inactive. Moreover, the obtained Au-Rh nanoclusters are stable without any segregation during the catalytic reactions. We anticipate that the facile and effective approach demonstrated here will benefit the creation of advanced alloys for catalytic applications.

2 Results and discussion

2.1 Synthesis of a solid ligand

We began by synthesis of a solid ligand consisting of the rich N and O sites through pyrolysis of urea with a commercial carbon (MSC-30) at 548 K (denoted as *u*C-548, see the Electronic Supplementary Material (ESM) for details). Raman spectra show similar G and D bands for *u*C-548 and MSC-30, confirming that the structure of carbon framework is maintained (Fig. S1 in the ESM). The specific surface area of *u*C-548 decreases drastically compared to MSC-30 (Fig. S2 in the ESM), meaning that most of the pores of MSC-30 have been occupied by the functional groups or products derived from the thermal decomposition of urea. High-resolution X-ray photoelectron spectroscopy (XPS) was performed to determine the incorporated groups (Figs. S3 and S4 in the ESM). In addition to the similar peak of graphitic C at 284.6 eV in C 1s spectrum of MSC-30, there are two strong shoulders at 285.7 and 288.8 eV for *u*C-548, corresponding to a higher percentage of C–N, C–O and C=O sites [30]. The O 1s spectrum shows C=O, C–O and hydroxyl groups in *u*C-548 [31]. While no N signals are detected in the N 1s spectrum of MSC-30, the strong N signals are observed in the survey and N 1s spectrum of *u*C-548, indicating that the incorporated groups are rich in N and O. The incorporated N species are well-fitted as four different components: The peak at 401.1 eV is assigned to quaternary N, which is contributed by the thermally stable N species; the peak at 400.2 eV is attributed to N atoms in pyrrole-like configuration; the peak at 399.5 eV refers to N–H bonds in low-temperature stable amide and amine; and the peak at 398.7 eV is assigned to the pyridine-like N [31].

2.2 Solid-solution alloying of bulk-immiscible Au and Rh

In a further step, the Au-Rh system was chosen to demonstrate the effectiveness of solid ligands toward the solid-solution alloying of bulk-immiscible metals (Fig. 1, see the ESM for details). The powder X-ray diffraction (PXRD) measurements were carried out to investigate the crystal structures of the obtained Au_xRh_{1-x}/*u*C-548 samples, where x = 1.0, 0.9, 0.7, 0.5 and 0.3. As shown in Fig. 2(a), the broad peaks of Au_xRh_{1-x} clusters, which locate in between the characteristic peaks of the individual Au (JCPDS File No. 65-8601) and Rh (JCPDS File No. 05-0685) with marked shifting through varying the molar ratios of Au and Rh, indicate the alloying of Au and Rh. The electronic interactions between Au and Rh atoms were studied by the high-resolution XPS analysis (Fig. 2(b) and Fig. S5 in the ESM). The Au $4f_{7/2}$ peaks shift to the higher binding energy with the increase in Rh content, indicating the charge transfer between Au and Rh due to alloying. Although shifts are shown for the Rh $3d_{5/2}$ peaks of Au_xRh_{1-x}/*u*C-548 compared to Rh/*u*C-548, a clear variation trend in Rh 3d lines with the increase in Au content cannot be observed, due to the effect of the Rh(III) species. The effect of Rh on the electronic structure of Au is clearer in the Au 4f spectra, for which the observed upward shifts of around 0.4–0.9 eV indicate the internal diffusion of atomic Au into Rh. Moreover, to confirm the coordination information for Au and Rh atoms, the samples were investigated by synchrotron radiation based X-ray adsorption fine structure (XAFS) spectroscopy. Figure 2(c) shows the Au L_3-edge X-ray absorption near-edge structure (XANES) spectra of $Au_{0.5}Rh_{0.5}$/*u*C-548 and Au/*u*C-548 in reference to standard Au foil. The XANES spectra of $Au_{0.5}Rh_{0.5}$/*u*C-548 and Au/*u*C-548 have similar shapes to that recorded on Au foil, indicating the formation of metallic Au in alloyed $Au_{0.5}Rh_{0.5}$ and Au clusters. However, owing to the low coordination number of the Au–Au bond, the Au L_3 edge of Au in the alloyed $Au_{0.5}Rh_{0.5}$/*u*C-548 shifts to higher energy, and its white line becomes broader, compared to Au/*u*C-548 and Au foil. Processed by using a Fourier-transform (FT), the Au L_3-edge extended XAFS (EXAFS) was obtained (Fig. 2(d)). The Au–Rh bonds appear with the disappearance

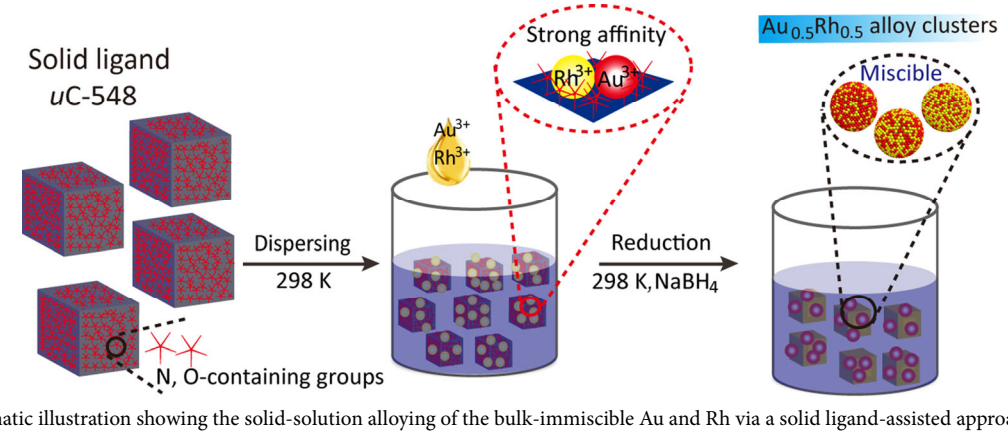

Figure 1 Schematic illustration showing the solid-solution alloying of the bulk-immiscible Au and Rh via a solid ligand-assisted approach.

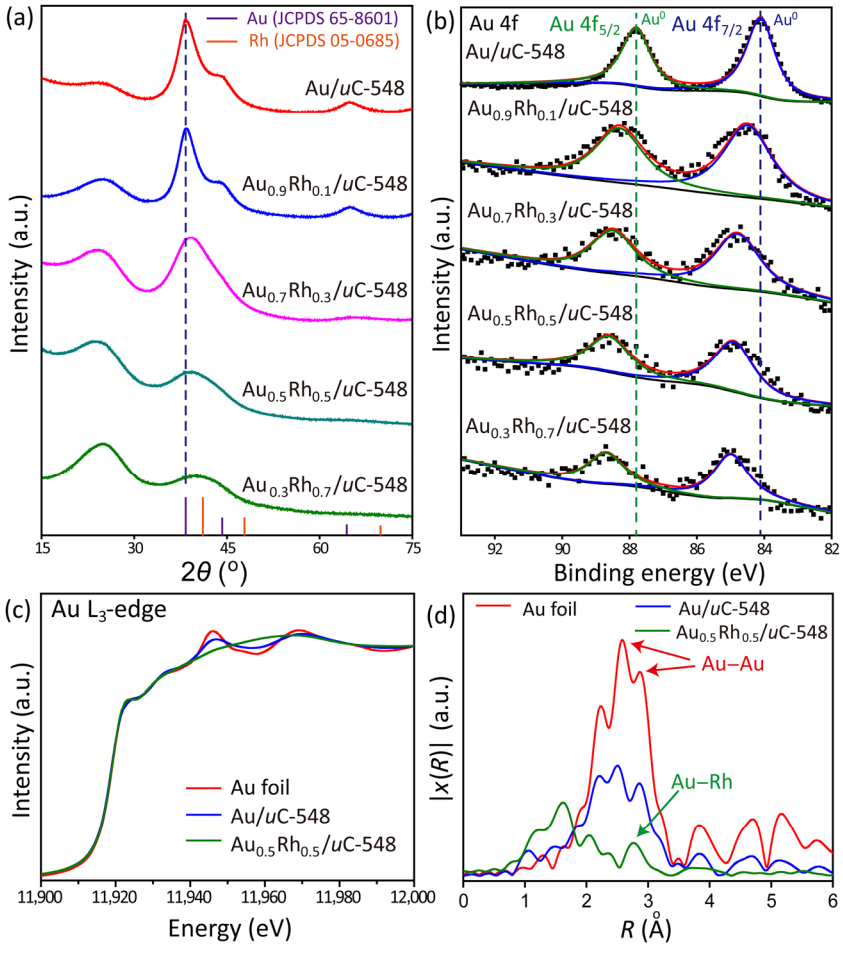

Figure 2 The PXRD patterns (a) and Au 4f core-level XPS spectra (b) recorded on *u*C-548 stabilized Au, $Au_{0.9}Rh_{0.1}$, $Au_{0.7}Rh_{0.3}$, $Au_{0.5}Rh_{0.5}$ and $Au_{0.3}Rh_{0.7}$ clusters. The normalized Au L_3-edge XANES spectra (c) and Fourier-transformed *r*-space data (d) of *u*C-548 stabilized $Au_{0.5}Rh_{0.5}$ and Au clusters compared with Au foil as reference.

of the Au–Au bonds in $Au_{0.5}Rh_{0.5}$/*u*C-548, suggesting that Rh atoms are mostly coordinated with Au atoms. The experimental EXAFS results are well consistent with the IFEFFIT fitting data (Fig. S6 and Table S1 in the ESM), further confirming the successful formation of Au-Rh alloys.

The transmission electron microscopy (TEM), high-angle annular dark-field scanning TEM (HAADF-STEM) and energy-dispersive X-ray spectroscopy (EDX) analyses were performed to clarify the morphology and alloying state of the obtained Au, $Au_{0.5}Rh_{0.5}$ and Rh clusters. Tiny and highly dispersed Au, $Au_{0.5}Rh_{0.5}$ and Rh clusters with the average size of ~ 1.5, 1.6 and 1.3 nm strongly interact with *u*C-548 surfaces, respectively (Fig. 3 and Fig. S7 in the ESM). The area scan of EDX indicates the co-existence of Au and Rh elements in a small region (Fig. S8 in the ESM). Considering that MCs are too small, the spot mode of EDX on multiple individual bimetallic nanoclusters was carried out, which can help determine the composition consistency by comparing the designated and actual weight ratios [32]. The actual weight ratios of the obtained $Au_{0.5}Rh_{0.5}$ nanoclusters are consistent with the expected ratio, indicating the strong interaction between Au and Rh atoms in bimetallic nanoclusters (Table S2 in the ESM). Similarly, EDX mapping and line scan results suggest that Au and Rh atoms are well-distributed in each nanocluster (Fig. S9 in the ESM). Clearly, the solid ligands are highly effective for immobilizing highly dispersed MCs, especially, the alloy clusters consisting of the bulk-immiscible elements.

2.3 Catalytic hydrogen evolution from formic acid

The Au_xRh_{1-x}/*u*C-548 was tested in the decomposition of liquid-phase FA to evaluate their catalytic activities. FA is well-known as a safe, nontoxic, easily accessible and highly stable hydrogen carrier that releases H_2 through the dehydrogenation process (HCOOH(l) → H_2 (g) + CO_2(g)) [33–41]. As shown in Fig. 4 and Fig. S10 in the ESM, monometallic Au/*u*C-548 shows poor activity while monometallic Rh/*u*C-548 shows no activity for this reaction. However, the introduction of Rh to Au leads to a significantly enhanced catalytic efficiency. All Au_xRh_{1-x}/*u*C-548 samples exhibit higher catalytic activity toward the H_2 evolution from FA than that of their monometallic parents (Fig. 4 and Fig. S10 in the ESM). Among all Au_xRh_{1-x}/*u*C-548 samples, $Au_{0.5}Rh_{0.5}$/*u*C-548 with a metal loading of 8.26 wt.% is found to be the most active catalysts, with which FA can be dehydrogenated completely (146 mL) within 1.67 min at 333 K, affording an initial turnover frequency (TOF) value as high as 2,297 h^{-1} (n(Au+Rh)/n(FA) = 0.02, Fig. S11 in the ESM). After that, the generated gas with a slow speed is attributed to the decomposition of SF. The gas chromatography (GC) analysis suggests the generated gas consisting of H_2 and CO_2 without a trace of CO (< 5 ppm), implying the high selectivity of Au_xRh_{1-x} alloy clusters (Fig. S12 in the ESM).

The catalytic activity exhibited by alloys usually involves the strong electronic effects of the constituent metals. As shown in XPS analyses (Fig. S13 in the ESM), Au/*u*C-548 and Rh/*u*C-548 show a small shift of Au $4f_{7/2}$ and Rh $3d_{5/2}$ peaks compared to bulk Au and Rh, respectively, while $Au_{0.5}Rh_{0.5}$/*u*C-548 shows large shifts of 0.8 and 0.4 eV for Au $4f_{7/2}$ and Rh $3d_{5/2}$ peaks due to alloying. Additionally, significant increases in the full-width at half maximum (FWHM) are observed for the Au $4f_{7/2}$ and Rh

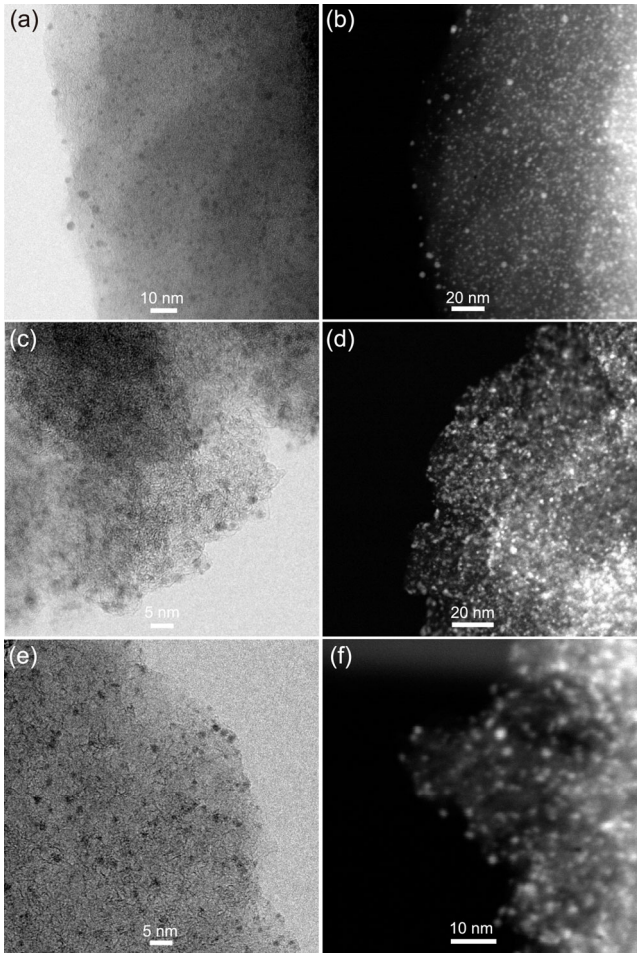

Figure 3 TEM and HAADF-STEM images of *u*C-548 stabilized (a) and (b) Au clusters, (c) and (d) $Au_{0.5}Rh_{0.5}$ clusters and (e) and (f) Rh clusters.

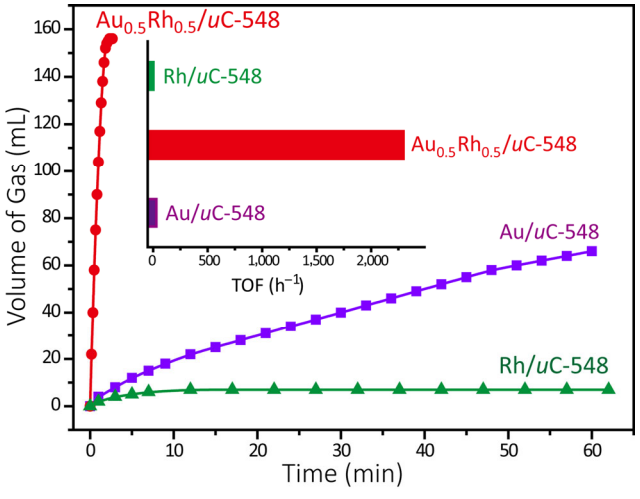

Figure 4 Volume of the generated gas vs. time for the dehydrogenation of FA over the Au/*u*C-548, $Au_{0.5}Rh_{0.5}$/*u*C-548 and Rh/*u*C-548 catalysts ($n_{(Au+Rh)}/n_{FA}$ = 0.02, n_{SF}/n_{FA} = 2.5, 333 K). Inset: corresponding TOF values of the catalysts.

$3d_{5/2}$ peaks of $Au_{0.5}Rh_{0.5}$/*u*C-548. Thus, the highly enhanced catalytic activity of $Au_{0.5}Rh_{0.5}$ clusters can be ascribed to the electronic structure changes of the constituent Au and Rh atoms resulted from the atomic interaction. To gain deep insights into the use of $Au_{0.5}Rh_{0.5}$/*u*C-548 for the catalytic dehydrogenation of FA, the reaction kinetics were investigated. As the reaction rate is constant at the beginning of the reaction (Fig. S14 in the ESM), the initial rates and TOFs are used to evaluate the effects from the temperature, base, FA and metal catalyst. Madon-Boudart test was performed to evaluate the significance of heat and mass-transfer effects [42, 43]. Similar TOFs are observed for $Au_{0.5}Rh_{0.5}$/*u*C-548 with different metal loadings at different temperatures, indicating the absence of heat transport limitations (Fig. S15 in the ESM). Increased gas release rates and TOF values are observed at elevated reaction temperatures (Fig. S16 in the ESM). The activation energy (E_a) calculated from the Arrhenius plot is 55.0 kJ·mol^{-1}. The $Au_{0.5}Rh_{0.5}$/*u*C-548 shows a very low activity towards the hydrogen generation from pure sodium formate (HCOONa, SF) (Fig. S17 in the ESM). The addition of SF boosts the gas release rate (Fig. S18 in the ESM), indicating that the catalytic dehydrogenation of FA is limited by the step involving metal-formate intermediates present at saturation condition. The initial concentrations of FA and metal also have obvious influence on the gas release rate (Figs. S19 and S20 in the ESM). On the basis of the slopes of double logarithmic plots recorded in dilute FA in aqueous solution, the observed rate law for the FA dehydrogenation has rate ~ $[metal]^1[SF]^{0.5}[FA]^{0.5}$. It means that two sites of the metal catalyst are activated by a single equivalent of SF for dehydrogenation of a single equivalent of FA, thus leading to half-order dependence on base and FA. Upon consideration of the above results, a possible reaction pathway is proposed (Fig. S21 in the ESM). The basic N sites on *u*C-548, as a proton scavenger, facilitate the O–H cleavage, leading to the formation of a metal-formate complex. The altered electronic structure of $Au_{0.5}Rh_{0.5}$ clusters facilitates the β-hydride elimination of metal-formate species, producing CO_2 and metal hydride species. Finally, H_2 is generated by the reaction of the hydride species with N sites, along with the regeneration of the zero-valent metal species.

Durability and stability are critical indicators for heterogeneous catalysts. The $Au_{0.5}Rh_{0.5}$/*u*C-548 catalysts maintain the outstanding catalytic activities for at least 7 cycles (Fig. S22 in the ESM). TEM and HAADF-STEM images reveal that the size and morphology of $Au_{0.5}Rh_{0.5}$ clusters in $Au_{0.5}Rh_{0.5}$/*u*C-548 after 7 cycles remain the same as those of the fresh catalysts (Fig. S23 in the ESM). PXRD and EDX spot model measurements show that there is no phase segregation in $Au_{0.5}Rh_{0.5}$ clusters during the catalytic reactions (Fig. S24 and Table S3 in the ESM). Thus, the construction of an appropriate solid ligand to achieve the solid-solution alloying of bulk-immiscible metals is very promising for the creation of advanced alloy catalysts.

2.4 Investigation of the role of solid ligands

The role of *u*C-548 in the alloying and stabilization of ultrafine Au_xRh_{1-x} clusters aroused our interest. In general, the atomic interaction of well-defined miscible metals in alloys can be easily achieved by simultaneously reducing the metal precursors, whereas for the bulk-immiscible metallic elements, severe phase segregation will occur owing to their complex alloying process [9]. To prove this point, control experiments with the support-free and carbon-supported $Au_{0.5}Rh_{0.5}$ NPs were performed. The support-free $Au_{0.5}Rh_{0.5}$ NPs are too large with severe aggregation and phase segregation, and thus exhibit no activity for the dehydrogenation of FA (Figs. S25–S27 in the ESM). The carbon-supported $Au_{0.5}Rh_{0.5}$ NPs ($Au_{0.5}Rh_{0.5}$/MSC-30) are also too large with severe phase separation and non-uniform distribution (Figs. S28 and S29, and Table S4 in the ESM) owing to the weak affinity between carbon surfaces and metal precursors. As expected, $Au_{0.5}Rh_{0.5}$/MSC-30 show a poor catalytic activity, with which the FA dehydrogenation is uncompleted even in 40 min (Fig. S30 in the ESM). Another control experiment with the polyol reduction method, in which polyvinylpyrrolidone (PVP) was used as surface capping agent to control the NP nucleation

and growth, was further performed. The PXRD pattern reveals that the obtained bimetallic NPs are composed of multiple components (Fig. S31 in the ESM). The subsequent catalysis experiments indicate that the obtained MNPs possess low catalytic kinetics, owing to the large amount of capped metal sites, and the weak synergistic interaction between Au and Rh (Fig. S32 in the ESM). In addition, a control experiment with the use of polyethylene glycol (PEG8000) to control the NP nucleation and growth was performed. The obtained $Au_{0.5}Rh_{0.5}$ NPs show poor catalytic activities for FA dehydrogenation (Fig. S33 in the ESM). It is no doubt that the solid-solution alloying of the immiscible Au-Rh system can be attributed to the use of *u*C-548 to replace the traditional solid supports and organic capping agents.

The high-resolution XPS spectra provide the local information of the interactions between the N, O-sites of *u*C-548 and metals. Figure 5(b) compares the Rh 3d spectra for the unreduced $Au^{3+}Rh^{3+}$/*u*C-548 and the reduced $Au_{0.5}Rh_{0.5}$/*u*C-548 samples. The trivalent Rh species in the $Au^{3+}Rh^{3+}$/*u*C-548 samples undergo a transformation to zero-valent Rh components assigned to $Au_{0.5}Rh_{0.5}$ clusters upon reduction using $NaBH_4$. However, a fraction of trivalent Rh species with a shift of 0.2 eV still exists in $Au_{0.5}Rh_{0.5}$/*u*C-548, which can be ascribed to the formed complexes between the N sites and Rh^{3+} ions. As shown in Fig. 5(c) and Table S5 in the ESM, the loading and reduction of metal precursors cause a modification of the N 1s species: a) The pyridinic N and N–H components decease while pyrrolic N components increase with the loading of metal precursors due to the strong interactions between metal ions and N; b) the pyrrolic N components decrease while the pyridinic N and N–H components increase after the reduction of metal precursors, similar to the starting *u*C-548, which can be attributed to the mobility of $Au_{0.5}Rh_{0.5}$ clusters during reduction where the metal ion-coordinated N species can become surface exposed; and c) the pyridinic N, N–H and pyrrolic N species shift to low values resulting from the charge transfer from metals, indicating the strong affinity between the N sites and MCs. The O 1s spectra are also modified: a) The relative abundance of the C=O components decreases with the loading of metal precursors, which can be attributed to the strong electrostatic adsorption of C=O to metal precursors, b) the C=O components increase after the reduction of metal precursors due to the mobility of MCs, and c) the C–O and C=O species shift to low values indicating the strong affinity between the O sites and MCs (Fig. 5(d)). On the other hand, the electrostatic interactions, through the strong electrostatic adsorption from the charged C=O sites or OH groups to oppositely charged metal precursors, are usually suggested to be the main driving force for NP nucleation and growth on solid supports. A strong electrostatic interaction can be achieved by adjusting the pH value of aqueous solution relative to the surface point of zero charge (PZC). Here, a PZC value of 6.1 was determined for *u*C-548 (Fig. S34 in the ESM), i.e., the surface of *u*C-548 is positive below pH of 6.1, and negative above pH of 6.1. It is reasonable to assume that a pH range near 6.1 is appropriate for this wok because the high pH allows the cationic Rh(III) to be absorbed while the low pH drives the anionic $AuCl_4$(I) to be absorbed by the solid ligand. Although alloyed clusters can be obtained by different pH

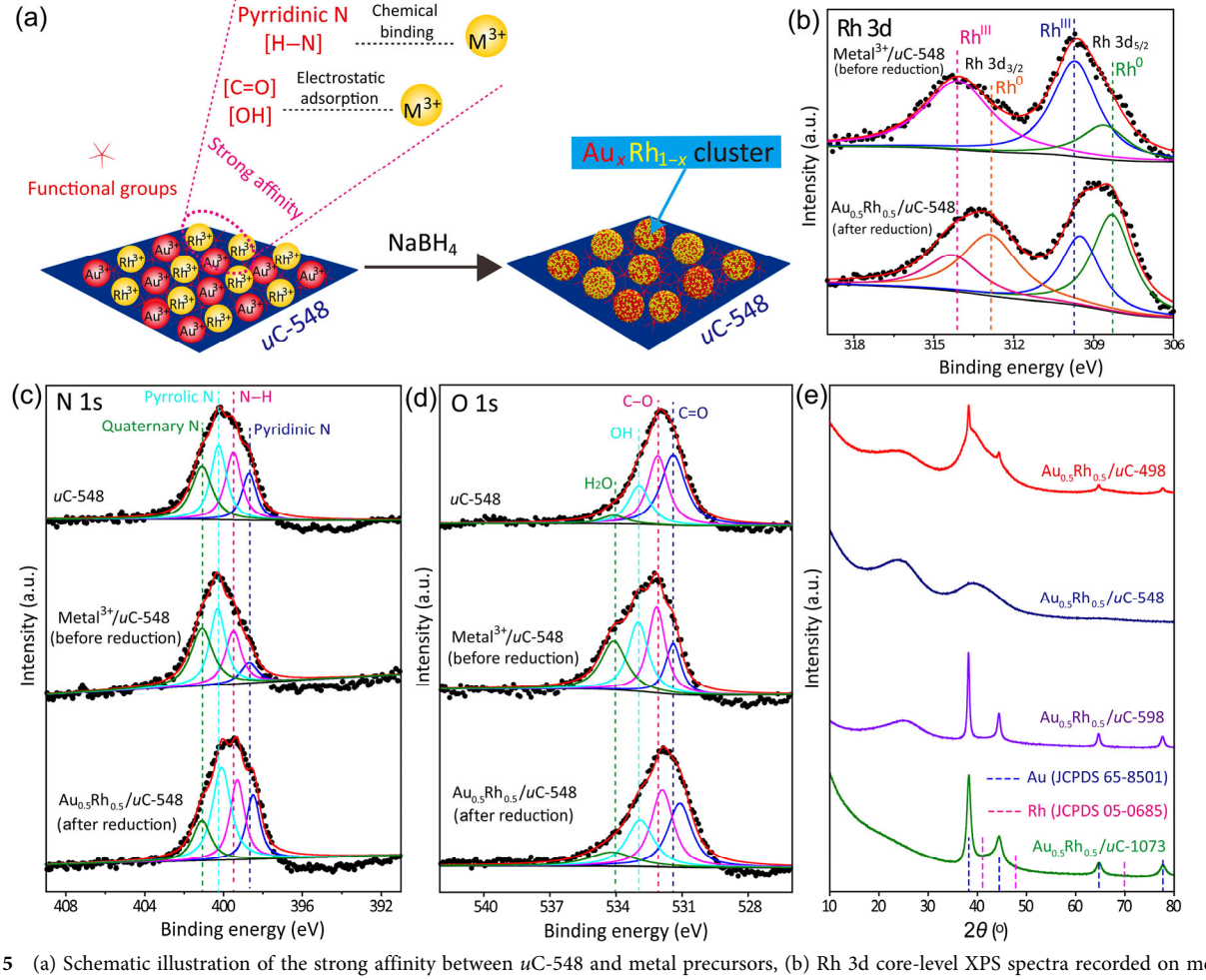

Figure 5 (a) Schematic illustration of the strong affinity between *u*C-548 and metal precursors, (b) Rh 3d core-level XPS spectra recorded on metal^{3+}/*u*C-548 and $Au_{0.5}Rh_{0.5}$/*u*C-548, (c) N 1s and (d) O 1s core-level XPS spectra of *u*C-548, metal^{3+}/*u*C-548 and $Au_{0.5}Rh_{0.5}$/*u*C-548, and (e) PXRD patterns of $Au_{0.5}Rh_{0.5}$/*u*C-498, $Au_{0.5}Rh_{0.5}$/*u*C-548, $Au_{0.5}Rh_{0.5}$/*u*C-598 and $Au_{0.5}Rh_{0.5}$/*u*C-1073.

conditions, as expected, the highest catalytic activity is observed for $Au_{0.5}Rh_{0.5}$/*u*C-548 prepared at pH 7 (Figs. S35 and S36 in the ESM). Clearly, *u*C-548 with rich N and O sites has strong chemical binding ability and electrostatic absorption to Au and Rh precursors, which can facilitate the solid-solution alloying of bulk-immiscible Au and Rh during reduction process and stabilize the resultant alloy clusters, and finally, promote catalysis by downscaling the alloys, offering more available active sites, and benefiting the dispersion of $Au_{0.5}Rh_{0.5}$ clusters and their intermetallic synergetic effects (Fig. 5(a)).

To gain further insights into the roles of *u*C-548, three control solid ligands, named as *u*C-498, *u*C-598 and *u*C-1073, were synthesized at different temperatures for achieving the solid-solution alloying of the immiscible Au and Rh, respectively. As revealed by PXRD patterns (Fig. 5(e)), $Au_{0.5}Rh_{0.5}$/*u*C-498, $Au_{0.5}Rh_{0.5}$/*u*C-598 and $Au_{0.5}Rh_{0.5}$/*u*C-1073 show overlapped diffraction peaks corresponding to the severe phase segregation in MNPs compared to $Au_{0.5}Rh_{0.5}$/*u*C-548, illustrating that the heating temperature of urea is crucial for enhancing the affinity of carbon surfaces to metal species, and 548 K is the optimal temperature for constructing solid ligands. Consequently, $Au_{0.5}Rh_{0.5}$/*u*C-548 shows much higher catalytic activities than $Au_{0.5}Rh_{0.5}$/*u*C-498, $Au_{0.5}Rh_{0.5}$/*u*C-598 and $Au_{0.5}Rh_{0.5}$/*u*C-1073 (Fig. S37 in the ESM). Interestingly, the elemental analysis and XPS spectra suggest that the maximum amount of N and O components were incorporated on carbon surfaces at 548 K (Tables S6 and S7 in the ESM) [44]. That is, the obtained maximum amount of appropriate N and O components such as pyridinic N, N–H, C=O and hydroxyl groups could significantly and simultaneously enhance the chemical binding ability and electrostatic adsorption of the two metal precursors to solid ligands, and thus achieve the solid-solution alloying of the entirely immiscible Au and Rh in MCs.

3 Conclusions

In conclusion, we demonstrate a simple and effective solid ligand-assisted methodology for achieving the solid-solution alloying of bulk-immiscible Au and Rh in plenty of clean, ultrafine and highly dispersed MCs. The strong interaction between the entirely immiscible Au and Rh produces the significantly enhanced catalytic activities for solid-solution nanoclusters compared to their monometallic parents. The solid-solution alloy nanoclusters of Au and Rh is stable without any segregation during catalytic reactions. Our success relies on simultaneously and significantly enhancing the chemical binding ability and electrostatic adsorption of solid ligands to the two different metal precursors; no additional organic ligands/capping agents were needed. We anticipate that the approach demonstrated here for constructing solid-solution nanoclusters containing the entirely immiscible metals will benefit the creation of advanced metal alloys for catalytic applications in future.

Acknowledgements

The authors thank METI, AIST and Kobe University for financial support, and Dr. Takeyuki Uchida for TEM measurements. X. C. Y. is grateful to the MEXT and CSC for a PhD scholarship.

Electronic Supplementary Material: Supplementary material (experimental details; Raman spectra; N_2 sorption isotherms; XPS spectra; EXAFS spectra; TEM images; HAADF-STEM images; GC data; catalytic reactions for FA dehydrogenation) is available in the online version of this article at https://doi.org/10.1007/s12274-019-2579-1.

References

[1] Buchwalter, P.; Rosé, J.; Braunstein, P. Multimetallic catalysis based on heterometallic complexes and clusters. *Chem. Rev.* **2015**, *115*, 28–126.
[2] Zhu, D. D.; Liu, J. L.; Qiao, S. Z. Recent advances in inorganic heterogeneous electrocatalysts for reduction of carbon dioxide. *Adv. Mater.* **2016**, *28*, 3423–3452.
[3] Fan, Z. X.; Zhang, H. Template synthesis of noble metal nanocrystals with unusual crystal structures and their catalytic applications. *Acc. Chem. Res.* **2016**, *49*, 2841–2850.
[4] Zhao, X. J.; Dai, L.; Qin, Q.; Pei, F.; Hu, C. Y.; Zheng, N. F. Self-supported 3D PdCu alloy nanosheets as a bifunctional catalyst for electrochemical reforming of ethanol. *Small* **2017**, *13*, 1602970.
[5] Xu, L.; Liang, H. W.; Yang, Y.; Yu, S. H. Stability and reactivity: Positive and negative aspects for nanoparticle processing. *Chem. Rev.* **2018**, *118*, 3209–3250.
[6] Yang, X. C.; Xu, Q. Gold-containing metal nanoparticles for catalytic hydrogen generation from liquid chemical hydrides. *Chin. J. Catal.* **2016**, *37*, 1594–1599.
[7] Kumar, A.; Yang, X. C.; Xu, Q. Ultrafine bimetallic Pt–Ni nanoparticles immobilized on 3-dimensional N-doped graphene networks: A highly efficient catalyst for dehydrogenation of hydrous hydrazine. *J. Mater. Chem. A* **2019**, *7*, 112–115.
[8] Yang, X. C.; Pachfule, P.; Chen, Y.; Tsumori, N.; Xu, Q. Highly efficient hydrogen generation from formic acid using a reduced graphene oxide-supported AuPd nanoparticle catalyst. *Chem. Commun.* **2016**, *52*, 4171–4174.
[9] Christensen, A.; Stoltze, P.; Norskov, J. K. Size dependence of phase separation in small bimetallic clusters. *J. Phys.: Condens. Matter* **1995**, *7*, 1047–1057.
[10] Essinger-Hileman, E. R.; DeCicco, D.; Bondi, J. F.; Schaak, R. E. Aqueous room-temperature synthesis of Au-Rh, Au-Pt, Pt-Rh, and Pd-Rh alloy nanoparticles: Fully tunable compositions within the miscibility gaps. *J. Mater. Chem.* **2011**, *21*, 11599–11604.
[11] García, S.; Zhang, L.; Piburn, G. W.; Henkelman, G.; Humphrey, S. M. Microwave synthesis of classically immiscible rhodium-silver and rhodium-gold alloy nanoparticles: Highly active hydrogenation catalysts. *ACS Nano* **2014**, *8*, 11512–11521.
[12] Chen, L. Y.; Chen, X. D.; Liu, H. L.; Li, Y. W. Encapsulation of mono- or bimetal nanoparticles inside metal-organic frameworks via *in situ* incorporation of metal precursors. *Small* **2015**, *11*, 2642–2648.
[13] Zhang, Q.; Kusada, K.; Wu, D. S.; Yamamoto, T.; Toriyama, T.; Matsumura, S.; Kawaguchi, S.; Kubota, Y.; Kitagawa, H. Selective control of fcc and hcp crystal structures in Au-Ru solid-solution alloy nanoparticles. *Nat. Commun.* **2018**, *9*, 510.
[14] Liu, H. L.; Chang, L. N.; Bai, C. H.; Chen, L. Y.; Luque, R.; Li, Y. W. Controllable encapsulation of "clean" metal clusters within MOFs through kinetic modulation: Towards advanced heterogeneous nanocatalysts. *Angew. Chem., Int. Ed.* **2016**, *55*, 5019–5023.
[15] Liu, B.; Yao, H. Q.; Song, W. Q.; Jin, L.; Mosa, I. M.; Rusling, J. F.; Suib, S. L.; He, J. Ligand-free noble metal nanocluster catalysts on carbon supports via "soft" nitriding. *J. Am. Chem. Soc.* **2016**, *138*, 4718–4721.
[16] Gao, W. B.; Wang, P. K.; Guo, J. P.; Chang, F.; He, T.; Wang, Q. R.; Wu, G. T.; Chen, P. Barium hydride-mediated nitrogen transfer and hydrogenation for ammonia synthesis: A case study of cobalt. *ACS Catal.* **2017**, *7*, 3654–3661.
[17] Yang, X. C.; Sun, J. K.; Kitta, M.; Pang, H.; Xu, Q. Encapsulating highly catalytically active metal nanoclusters inside porous organic cages. *Nat. Catal.* **2018**, *1*, 214–220.
[18] Liu, G. Y.; Sheng, Y.; Ager, J. W.; Kraft, M.; Xu, R. Research advances towards large-scale solar hydrogen production from water. *EnergyChem* **2019**, *1*, 100014.
[19] Zheng, Y.; Jiao, Y.; Zhu, Y. H.; Li, L. H.; Han, Y.; Chen, Y.; Du, A. J.; Jaroniec, M.; Qiao, S. Z. Hydrogen evolution by a metal-free electrocatalyst. *Nat. Commun.* **2014**, *5*, 3783.
[20] Kohl, M.; Borrmann, F.; Althues, H.; Kaskel, S. Hard carbon anodes and novel electrolytes for long-cycle-life room temperature sodium-sulfur full cell batteries. *Adv. Energy Mater.* **2016**, *6*, 1502185.
[21] Hou, Y.; Qiu, M.; Zhang, T.; Ma, J.; Liu, S. H.; Zhuang, X. D.; Yuan, C.; Feng, X. L. Efficient electrochemical and photoelectrochemical water splitting by a 3D nanostructured carbon supported on flexible

exfoliated graphene foil. *Adv*. *Mater*. **2017**, *29*, 1604480.
[22] Pachfule, P.; Yang, X. C.; Zhu, Q. L.; Tsumori, N.; Uchida, T.; Xu, Q. From Ru nanoparticle-encapsulated metal-organic frameworks to highly catalytically active Cu/Ru nanoparticle-embedded porous carbon. *J*. *Mater*. *Chem*. *A* **2017**, *5*, 4835–4841.
[23] He, L.; Weniger, F.; Neumann, H.; Beller, M. Synthesis, characterization, and application of metal nanoparticles supported on nitrogen-doped carbon: Catalysis beyond electrochemistry. *Angew. Chem., Int. Ed.* **2016**, *55*, 12582–12594.
[24] Zhong, S.; Kitta, M.; Xu, Q. Hierarchically porous carbons derived from metal-organic framework/chitosan composites for high-performance supercapacitors. *Chem*. *Asian J*. **2019**, *14*, 3583–3589.
[25] Lu, L. L.; Wu, B. Y.; Shi, W.; Chen, P. Metal-organic framework-derived heterojunctions as nanocatalysts for photocatalytic hydrogen production. *Inorg*. *Chem*. *Front*., in press, DOI: 10.1039/C9QI00964G.
[26] Huang, J. H.; Akita, T.; Faye, J.; Fujitani, T.; Takei, T.; Haruta, M. Propene epoxidation with dioxygen catalyzed by gold clusters. *Angew. Chem., Int. Ed.* **2009**, *48*, 7862–7866.
[27] Zhong, R. Y.; Sun, K. Q.; Hong, Y. C.; Xu, B. Q. Impacts of organic stabilizers on catalysis of Au nanoparticles from colloidal preparation. *ACS Catal*. **2014**, *4*, 3982–3993.
[28] Sun, J. K.; Zhan, W. W.; Akita, T.; Xu, Q. Toward homogenization of heterogeneous metal nanoparticle catalysts with enhanced catalytic performance: Soluble porous organic cage as a stabilizer and homogenizer. *J*. *Am*. *Chem*. *Soc*. **2015**, *137*, 7063–7066.
[29] Okamoto, H.; Massalski, T. B. The Au-Rh (gold-rhodium) system. *Bull*. *Alloy Phase Diagrams* **1984**, *5*, 384–387.
[30] Richardson, M. J.; Johnston, J. H. Sorption and binding of nano-crystalline gold by Merino wool fibres—An XPS study. *J*. *Colloid Interface Sci*. **2007**, *310*, 425–430.
[31] Arrigo, R.; Hävecker, M.; Wrabetz, S.; Blume, R.; Lerch, M.; McGregor, J.; Parrott, E. P. J.; Zeitler, J. A.; Gladden, L. F.; Knop-Gericke, A. et al. Tuning the acid/base properties of nanocarbons by functionalization via amination. *J*. *Am*. *Chem*. *Soc*. **2010**, *132*, 9616–9630.
[32] Wong, A.; Liu, Q.; Griffin, S.; Nicholls, A.; Regalbuto, J. R. Synthesis of ultrasmall, homogeneously alloyed, bimetallic nanoparticles on silica supports. *Science* **2017**, *358*, 1427–1430.
[33] Moret, S.; Dyson, P. J.; Laurenczy, G. Direct synthesis of formic acid from carbon dioxide by hydrogenation in acidic media. *Nat*. *Commun*. **2014**, *5*, 4017.
[34] Wang, W. H.; Ertem, M. Z.; Xu, S. A.; Onishi, N.; Manaka, Y.; Suna, Y.; Kambayashi, H.; Muckerman, J. T.; Fujita, E.; Himeda, Y. Highly robust hydrogen generation by bioinspired Ir complexes for dehydrogenation of formic acid in water: Experimental and theoretical mechanistic investigations at different pH. *ACS Catal*. **2015**, *5*, 5496–5504.
[35] Mellmann, D.; Sponholz, P.; Junge, H.; Beller, M. Formic acid as a hydrogen storage material-development of homogeneous catalysts for selective hydrogen release. *Chem*. *Soc*. *Rev*. **2016**, *45*, 3854–3988.
[36] Sun, Q. M.; Wang, N.; Bing, Q. M.; Si, R.; Liu, J. Y.; Bai, R. S.; Zhang, P.; Jia, M. J.; Yu, J. H. Subnanometric hybrid Pd-M$(OH)_2$, M = Ni, Co, clusters in zeolites as highly efficient nanocatalysts for hydrogen generation. *Chem* **2017**, *3*, 477–493.
[37] Li, Z. P.; Xu, Q. Metal-nanoparticle-catalyzed hydrogen generation from formic acid. *Acc*. *Chem*. *Res*. **2017**, *50*, 1449–1458.
[38] Sordakis, K.; Tang, C. H.; Vogt, L. K.; Junge, H.; Dyson, P. J.; Beller, M.; Laurenczy, G. Homogeneous catalysis for sustainable hydrogen storage in formic acid and alcohols. *Chem*. *Rev*. **2018**, *118*, 372–433.
[39] Mori, K.; Sano, T.; Kobayashi, H.; Yamashita, H. Surface engineering of a supported PdAg catalyst for hydrogenation of CO_2 to formic acid: Elucidating the active Pd atoms in alloy nanoparticles. *J*. *Am*. *Chem*. *Soc*. **2018**, *140*, 8902–8909.
[40] Hong, C. B.; Zhu, D. J.; Ma, D. D.; Wu, X. T.; Zhu, Q. L. An effective amino acid-assisted growth of ultrafine palladium nanocatalysts toward superior synergistic catalysis for hydrogen generation from formic acid. *Inorg*. *Chem*. *Front*. **2019**, *6*, 975–981.
[41] Li, S. J.; Zhou, Y. T.; Kang, X.; Liu, D. X.; Gu, L.; Zhang, Q. H.; Yan, J. M.; Jiang, Q. A simple and effective principle for a rational design of heterogeneous catalysts for dehydrogenation of formic acid. *Adv*. *Mater*. **2019**, *31*, 1806781.
[42] Madon, R. J.; Boudart, M. Experimental criterion for the absence of artifacts in the measurement of rates of heterogeneous catalytic reactions. *Ind*. *Eng*. *Chem*. *Fundamen*. **1982**, *21*, 438–447.
[43] Singh, U. K.; Vannice, M. A. Kinetic and thermodynamic analysis of liquid-phase benzene hydrogenation. *AIChE J*. **1999**, *45*, 1059–1071.
[44] Schaber, P. M.; Colson, J; Higgins, S.; Thielen, D.; Anspach, B.; Brauer, J. Thermal decomposition (pyrolysis) of urea in an open reaction vessel. *Thermochim*. *Acta* **2004**, *424*, 131–142.